

THE UV SPECTRUM OF THE ULTRACOOOL DWARF LSR J1835+3259 OBSERVED WITH THE HUBBLE SPACE TELESCOPE

JOACHIM SAUR,¹ CHRISTIAN FISCHER,¹ ALEXANDRE WENNMACHER,¹ PAUL D. FELDMAN,² LORENZ ROTH,³
DARRELL F. STROBEL,⁴ AND ANSGAR REINERS⁵

¹*Institut für Geophysik und Meteorologie
Universität zu Köln
Albertus-Magnus-Platz
Cologne, 50923, Germany*

²*Department of Physics and Astronomy
The Johns Hopkins University
Baltimore*

MD, USA

³*School of Electrical Engineering
Royal Institute of Technology KTH
Stockholm*

Sweden

⁴*Department of Earth and Planetary Sciences, and Department of Physics and Astronomy
The Johns Hopkins University
Baltimore*

MD, USA

⁵*Institut für Astrophysik
Georg-August-Universität
Friedrich-Hund-Platz 1
37077 Göttingen*

Germany

ABSTRACT

An interesting question about ultracool dwarfs recently raised in the literature is whether their emission is purely internally driven or partially powered by external processes similar to planetary aurora known from the solar system. In this work we present Hubble Space Telescope observations of the energy fluxes of the M8.5 ultracool dwarf LSR J1835+3259 throughout the UV. The obtained spectra reveal that the object is generally UV-fainter compared to other earlier-type dwarfs. We detect the Mg II doublet at 2800 Å and constrain an average flux throughout the Near-UV. In the Far-UV without Lyman alpha, the ultracool dwarf is extremely faint with an energy output at least a factor of 1000 smaller as expected from auroral emission physically similar to that on Jupiter. We also detect the red wing of the Lyman alpha emission. Our overall finding is that the observed UV spectrum of LSR J1835+3259 resembles the spectrum of mid/late-type M-dwarf stars relatively well, but it is distinct from a spectrum expected from Jupiter-like auroral processes.

Keywords: stars: individual LSR J1835+3259 — ultraviolet: stars — stars: low-mass — brown dwarfs

1. INTRODUCTION

LSR J1835 + 3259 is an ultracool dwarf of spectral type M8.5, which is located 5.6 pc away from Earth in the constellation Lyra (Reid et al. 2003; Lépine et al. 2003; Hallinan et al. 2008; Deshpande et al. 2012). In the Hertzsprung-Russell diagram it is positioned near the end of the main sequence. In that region the X-ray energy, indicative for the presence of a magnetically heated corona, drops by two orders of magnitude over a small range in spectral type (Hallinan et al. 2015). LSR J1835 + 3259 is a fast rotator with a period of 2.84 hours. Its emission has been observed to be periodic at radio wavelengths, in optical bands and the H- α (Hallinan et al. 2008; Berger et al. 2008; Hallinan et al. 2015).

The dwarf LSR J1835+3259 possesses a strong magnetic field with values of ~ 0.2 Tesla derived from radio observations (Hallinan et al. 2015). Observations of NIR polarized and optical emission with the Keck telescope based on Zeeman signatures demonstrated that its magnetic field is at least 0.51 Tesla and covers at least 11% of its visible surface (Berdyugina et al. 2017; Kuzmychov et al. 2017). These authors derive from the Keck observations an effective temperature of $T_{eff} = 2800 \pm 30$ K and log gravity acceleration of $\log g = 4.50 \pm 0.05$. Based on evolutionary models, Berdyugina et al. (2017) infer a mass of $M = 55 \pm 4 M_J$, a radius of $R = 2.1 \pm 0.1 R_J$, and an age $t = 22 \pm 4$ Myr (with M_J and R_J the mass and radius of Jupiter, respectively). Therefore, Berdyugina et al. (2017) and Kuzmychov et al. (2017) conclude that LSR J1835+3259 is a young brown dwarf at the end of its accretion phase. We note, however, that at this young age, brown dwarfs exhibit a strong spectroscopic absorption feature from Li at 6708 Å. Brown dwarfs need a few 10–100 Myr to deplete Li, which makes the Li test a strong indicator for the age of a young object (Basri 2000). In LSR J1835+3259 no significant absorption of Li was found by Reiners & Basri (2009) in their high-resolution spectra, which appears to be inconsistent with the parameters derived by Berdyugina et al. (2017). Thus, the brown dwarf status of LSR J1835+3259 is inconclusive. In this work, the object is therefore referred to as ultracool dwarf. They are defined by spectral type M7 and later and thus can include stars at the end of the main sequence and substellar brown dwarfs (see e.g., Reiners & Basri 2009; Pineda et al. 2017). However, the mass of LSR J1835+3259 is of little importance for our study although a determination of its age would be extremely useful for our understanding of low mass object evolution.

Low mass stars including ultracool dwarfs have been extensively studied throughout the electromagnetic wavelength range including many studies at various UV wavelengths (e.g., Hawley & Johns-Krull 2003; Walkowicz et al. 2008; Walkowicz & Hawley 2009; France et al. 2012; Shkolnik et al. 2014). These objects can experience persistent internal heating of their coronal plasma to over 10^6 K. This heating above the photosphere is often thought to occur through dissipation of wave energy and is related to strong and localized magnetic field structures, such as loops (e.g., Pineda et al. 2017). Late-type M-dwarfs have also been shown to display flare activity, which additionally can contribute to the coronal heating (e.g., Hallinan et al. 2008; Reiners & Basri 2008, 2009, 2010). Very recently Ly- α has been detected on the very late-type M8 dwarf star Trappist-1 by Bourrier et al. (2017a,b). Trappist-1 is the coldest M dwarf star with known Ly- α emission. It possesses an effective temperature of 2550 ± 55 K (Gillon et al. 2016) with a Ly- α flux of $0.05 \text{ erg s}^{-1} \text{ cm}^{-2}$ at 1 AU from the star (Bourrier et al. 2017a). For confirmed brown dwarfs, no Far-UV emission has been detected, yet (Pineda et al. 2017). UV observations of brown dwarfs would be highly interesting because brown dwarfs possess properties in between those of low mass dwarf stars and very massive planets. They are massive enough to burn deuterium or lithium, but not massive enough to fuse hydrogen (e.g., Basri 2014). The atmospheres of brown dwarfs also display planet-like weather phenomena and clouds including species such as TiO (Crossfield et al. 2014; Helling & Casewell 2014).

An exciting new possibility about the ultracool dwarf LSR J1835+3259 was raised by Hallinan et al. (2015). The authors reported simultaneous radio and optical emissions from LSR J1835+3259, which was interpreted as auroral emission triggered by electron beams generated outside of the dwarf. This would be the first auroral emission observed outside the Solar System, but a confirmation of the proposed hypothesis is crucial. Hallinan et al. (2015) argue that the auroral emission on the dwarf could be powered by processes similar to Jupiter, i.e., by magnetospheric currents that couple energy into the upper atmosphere. The nature of this emission would then be fundamentally different compared to the emission from stars like the Sun, which is powered by internal processes, e.g., by magnetic processes that occur in their convection zones. The conclusions in Hallinan et al. (2015) have been reached by detailed modeling of the observed light curves. The derived power emitted at radio wavelength is $10^{22} \text{ erg s}^{-1}$, which requires 10^{24} to $10^{26} \text{ erg s}^{-1}$ of available power in electron beams. The Balmer H- α line emission amounts to a total of $2.5 \times 10^{24} \text{ erg s}^{-1}$. No X-Ray emission associated with the presence of a magnetically heated corona has been observed on LSR J1835 + 3259 by the Chandra Observatory (Berger et al. 2008). Near/Mid-ultraviolet emissions around 2600 Å with

FWHM of 693 Å have marginally been detected with the SWIFT 30 cm telescope (Berger et al. 2008). The integrated NUV flux however still amounts to a total of 2.5×10^{25} erg s⁻¹.

Auroral phenomena and electromagnetic coupling in extrasolar magnetospheres and astrospheres is a topic of growing interest from the observational side (e.g., Shkolnik et al. 2003, 2008; Poppenhaefer & Schmitt 2011; France et al. 2013; Pineda et al. 2017) and the theoretical side (e.g., Cuntz et al. 2000; Ip et al. 2004; Preusse et al. 2005; Lanza 2009; Cohen et al. 2009; Saur et al. 2013; Strugarek et al. 2015; Saur 2017). Whereas this body of work refers to the more general auroral and electromagnetic coupling of planets and stars, auroral and related radio emission from brown dwarfs and ultracool stars specifically have been studied theoretically by, e.g., Schrijver (2009); Nichols et al. (2012); Turnpenney et al. (2017). In the latter two studies it has been assumed that the steady-state-current picture of the auroral processes of Jupiter can be carried over to the dwarfs.

Observations and modeling of auroral processes and the associated electromagnetic couplings have a long tradition in solar system research. From the knowledge in the solar system, aurorae need three components (e.g., Mauk & Bagenal 2012): (1) A generator, located in the planets magnetosphere, which produces electric current or more generally electromagnetic energy. The electric current and energy are continued along the object's magnetic field lines into the atmosphere/ionosphere. (2) An accelerator region energizes the low energy electrons (which in most cases carry the current) to energies up to keV or MeV energies. (3) The electrons in the form of beams finally precipitate onto the atmosphere where atoms and molecules serve as the screen from which emission over a broad spectral range spanning UV, visible to IR and radio wavelengths are excited by electron impact. Observations of the relative ratios of the emission intensities at these wavelengths and their temporal/spatial structure give essential insights into the three auroral components and thus into the plasma environment around planetary objects.

In the solar system, Jupiter is the most massive planet with the strongest magnetic field, which also possesses the solar system's most powerful aurora. Compared to LSR J1835 + 3259, Jupiter's magnetic field is weaker with a polar field of $\sim 10^{-3}$ T and Jupiter is a slower rotator with a period of 9.9 hours. Aurora on Jupiter has been extensively studied spatially and at all wavelengths with the following characteristic total energy fluxes (Bhardwaj & Gladstone 2000): X-Ray: $1-4 \times 10^{16}$ erg s⁻¹, Far-UV (800-1800 Å): $2 - 10 \times 10^{19}$ erg s⁻¹, visible (3850-10000 Å): $10 - 100 \times 10^{16}$ erg s⁻¹, IR: 50×10^{19} erg s⁻¹ and radio (10kHz to a few MHz): 10×10^{16} erg s⁻¹. Most of the energy in the visible is within the Balmer lines. The origin of the X-ray emission is not fully understood, but is thought to be generated by different processes compared to the aurora at other wavelengths (Gladstone et al. 2002). The Ly- α spectrum of Jupiter has been studied in detail by a series of authors (e.g., Clarke et al. 1989, 1994; Prangé et al. 1997). Jupiter's radio emission is caused by the electron cyclotron maser instability generated by its non-thermal, auroral electron distributions (e.g., Zarka 1998).

Jupiter's aurora has three qualitatively different spatial features. (1): The main auroral oval is generated by the breakdown of magnetospheric corotation, when the plasma originating from Jupiter's moon Io moves radially outward (e.g., Hill 2001; Clarke et al. 2002). This establishes a process, similar to magnetic braking at stars, which couples Jupiter to its magnetospheric plasma. Therefore Jupiter's rotational energy ultimately powers the emission of its main auroral oval. (2) The moons of Jupiter leave auroral imprints in Jupiter's atmosphere (e.g., Connerney et al. 1993; Clarke et al. 2002; Wannawichian et al. 2010; Bonfond et al. 2017; Saur et al. 2013). (3): Polar emission is the least understood and likely originates from the outermost region of its magnetosphere. Our understanding of Jupiter's aurora currently experiences a paradigm change with the NASA spacecraft JUNO in a polar orbit around Jupiter. Among the new findings are that the dominant part of the auroral electrons appears to be broad in their energy distribution and are accelerated towards and away from Jupiter simultaneously (e.g., Mauk et al. 2017; Ebert et al. 2017). This points to the importance of stochastic acceleration potentially powered by plasma waves as, e.g., evoked in Saur et al. (2003) compared to acceleration processes only related to large scale steady-state magnetospheric current systems.

In this work, we analyze the UV spectrum of the dwarf LSR J1835+3259 to further investigate its possible auroral emission. Therefore we will test whether the spectral energy density (SED) of LSR J1835+3259 scales similar to the auroral emission from Jupiter or similar to the emission from mid/late-type M stars. In section 2, we first present details of new observations by the Space Telescope Imaging Spectrograph (STIS) on the Hubble Space Telescope (HST) to characterize the spectrum of LSR J1835+3259 throughout the UV. We also detail our data analysis procedures to search for the very faint emission of the target within these observations. In section 3, we present and discuss the observed fluxes for various wavelength ranges. In section 4 we compare our results with the spectral properties of Jupiter and M-dwarfs and in section 5 we discuss our main findings.

2. OBSERVATIONS

The HST/STIS observations of LSR J1835+3259 (program ID 14617) are designed to search for auroral emission throughout the UV wavelength range. In Table 1, we summarize the details of the 9 STIS exposures taken during five consecutive orbits of HST. Orbit number 1, 4, 5 were dedicated to the Far-UV (FUV) emission, orbit 2 to the Near-UV (NUV) and orbit 3 to the Ly- α wings.

The data analysis in this work is based on the x2d files where spectral energy fluxes in $\text{erg s}^{-1} \text{cm}^{-2} \text{\AA}^{-1}$ are provided. Because of the extremely faint nature of the target in the UV, its position on the detector and in the resultant x2d files could not be determined by direct visual identification. To search for and to extract fluxes, we applied the following procedure. The nominal reference location of the target in the y direction is $y_{\text{ref,nom}}$. The associated row is calculated by $y_r = \text{integer}(y_{\text{ref,nom}} + 0.5)$. The x direction in the x2d files is the direction of dispersion, i.e., the direction of wavelength λ . We extract the fluxes f_{trace} in x direction along the trace within several rows above and below the reference location y_r . The flux per unit wavelength as function of column i_x or equivalently λ is given by

$$f_{\text{trace}}(\lambda) = \sum_{i_y=y_{\text{ref}}-n_1}^{y_{\text{ref}}+n_2} f(\lambda, i_y). \quad (1)$$

The average background flux per pixel f_{bg}^{px} is calculated from rows sufficiently above and below the rows where we expect flux from the target, i.e.,

$$f_{\text{bg}}^{px}(\lambda) = \left(\sum_{i_y=y_{\text{ref}}+a_1}^{y_{\text{ref}}+a_2} f(\lambda, i_y) + \sum_{i_y=y_{\text{ref}}-b_1}^{y_{\text{ref}}-b_2} f(\lambda, i_y) \right) / (a_2 - a_1 + 1 + b_2 - b_1 + 1) \quad (2)$$

with the positive integer numbers $n_1, n_2, a_1, a_2, b_1, b_2$. The value of these integers depend on the type of exposure (see Table 2). This procedure calculates a separate background for each column i_x . The reason is that the background fluxes change along the dispersion axis. We assume that the background flux characterizes the background along the trace and thus the net flux from the target as a function of wavelength is given by

$$f_{\text{net}}(\lambda) = f_{\text{trace}}(\lambda) - f_{\text{bg}}^{px}(\lambda) (n_2 - n_1 + 1). \quad (3)$$

Table 1. Exposure details of HST/STIS observations of LSR J1835+3259 (ID: 14617)

Orbit	Exp	Rootname	UT obs date ^a	UT obs time ^a	Exp time	Type	Grating	Disp	Slit width
#	#		yyyy-mm-dd	hh:mm:ss	sec			\AA/pixel	arcsec
1	1	od9x01010	2017-03-04	15:59:14	1083.2	FUV	G140L	0.584	0.2
1	2	od9x01020	2017-03-04	16:20:43	1084.2	FUV	G140L	0.584	0.2
2	3	od9x01030	2017-03-04	17:21:22	1395.2	NUV	G230L	1.548	0.2
2	4	od9x01040	2017-03-04	17:48:03	1394.2	NUV	G230L	1.548	0.2
3	5	od9x01050	2017-03-04	19:13:04	2020.2	Ly- α	G140M	0.053	0.05
4	6	od9x01060	2017-03-04	20:32:16	1395.2	FUV	G140L	0.584	0.2
4	7	od9x01070	2017-03-04	20:58:57	1394.2	FUV	G140L	0.584	0.2
5	8	od9x01080	2017-03-04	22:07:43	1395.2	FUV	G140L	0.584	0.2
5	9	od9x01090	2017-03-04	22:34:24	1394.2	FUV	G140L	0.584	0.2

^aAt exposure start.

The variance of the background for each pixel in an individual column i_x associated with a certain wavelength λ is given by

$$V^{px}(i_x) = \left(\sum_{y_{ref}+a_1}^{y_{ref}+a_2} (f(i_x, i_y) - f_{bg}^{px}(i_x))^2 + \sum_{y_{ref}-b_1}^{y_{ref}-b_2} (f(i_x, i_y) - f_{bg}^{px}(i_x))^2 \right) / (a_2 - a_1 + b_2 - b_1 + 1). \quad (4)$$

When we compare flux uncertainties with the net fluxes from the target f_{net} , the variance in each pixel V^{px} needs to be normalized to the number of rows, which have been used to calculate f_{net} . In case net fluxes within certain wavelength ranges are calculated, the variances of the individual columns, which contribute to the selected wavelength ranges, additionally need to be summarized to the total variance V . The resultant uncertainties are calculated based on the standard deviation $\sigma = \sqrt{V}$.

3. RESULTS

The results of our observations are now discussed separately for the three different types of observation, i.e., for the NUV wavelength range in subsection 3.1, the FUV wavelength range in subsection 3.2 and the Ly- α wavelength in subsection 3.3.

3.1. Near-UV

NUV observations were performed with STIS grating G230L within the wavelength range 1570 - 3180 Å. Observations were taken during orbit 2 with two exposures (see Exp # 3 and # 4 in Table 1). The net fluxes per Å along the trace for each exposure and the combined NUV exposures are shown in Figure 1. The net flux $f_{net}(\lambda)$ is calculated as described in section 2. In order to minimize the contribution of the background noise, the numbers of rows to calculate the net flux was kept at a relatively small value, i.e., 6 (see Table 2).

Due to the faint nature of the object in the UV, we independently check whether the detected NUV flux is indeed collocated with the target position. Therefore we display in Figure 2 the flux integrated along the dispersion direction between 2200 Å and 3015 Å as a function of row number where we added the neighboring row above and the one below, respectively, in order to reduce the scattering in the plot. The reference location of the target lies at row 601 indicated by the red vertical line. The maximum of the integrated flux approximately coincides with the reference location and thus confirms a detection of a surplus of NUV flux generated by LSR J1835+3259. The reference is located one row number higher compared to the maximum in Figure 2, which we adjust by our choice of coefficients in Table 2 when calculating spectra. A visual comparison with the integrated flux values of the neighboring traces shows that the surplus along the reference trace is roughly $3 - 4 \times 10^{-15}$ erg s⁻¹ cm⁻².

When we integrate the net fluxes displayed in Figure 1 between 2220 and 3150 Å, we find a total averaged flux from both exposures of $(3.9 \pm 0.58) \times 10^{-15}$ erg s⁻¹ cm⁻² (see also Table 3). This leads to an average flux per wavelength of $(4.1 \pm 0.61) \times 10^{-18}$ erg s⁻¹ cm⁻² Å⁻¹. This value is similar to that from previous observations of $(4.7 \pm 1.3) \times 10^{-18}$ erg s⁻¹ cm⁻² Å⁻¹ obtained with the SWIFT Telescope in the NUV (Berger et al. 2008).

In Figure 1, a spectral feature around 2800 Å is apparent in exposures # 3 and # 4. In Figure 3, we zoom into this spectral region and identify the feature as the Mg II doublet at 2796 and 2803 Å (e.g., Feldman et al. (1996); France et al. (2013)). In exposure #3 the double peak structure is better visible compared to the exposure #4. The total flux within the doublet between 2792 and 2807 Å is $(9.3 \pm 0.57) \times 10^{-16}$ erg s⁻¹ cm⁻² for exposure # 3 and

Table 2. Data analysis details: Row information used for calculation of net fluxes.

Type	y_r	n_1	n_2	a_1	a_2	b_1	b_2
NUV	601	-3	2	3	23	-24	-4
FUV	474	-2	4	5	45	-43	-3
Ly- α	488	-2	4	5	35	-33	-3

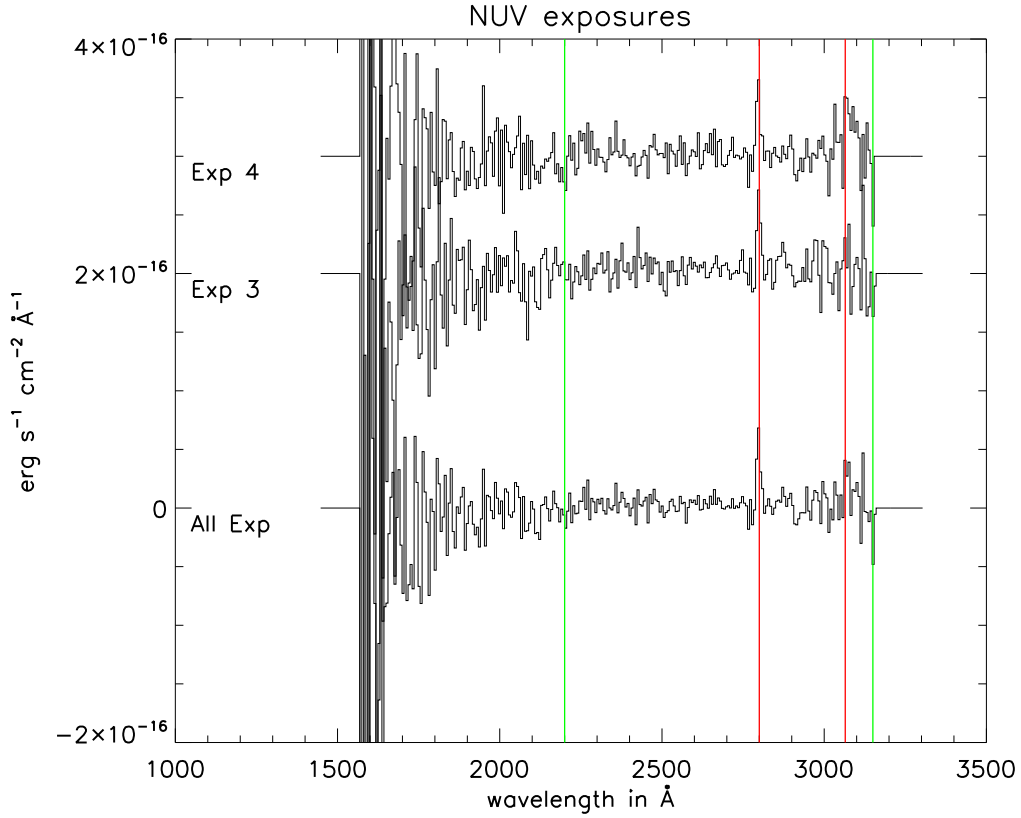


Figure 1. Net NUV flux per wavelength along trace for exposure # 3 and # 4 and combined exposure. Spectra are shifted for readability. The green vertical lines mark the wavelength range 2200 Å to 3150 Å over which we calculate the total FUV flux. The red vertical line at 2800 Å indicates the expected wavelength of Mg II emission and the red line at 3065 Å might be associated with TiO emission (see main text).

$(7.1 \pm 0.70) \times 10^{-16}$ erg s⁻¹ cm⁻² for exposure # 4. The fluxes measured during the two exposures are different at the approximately 1- σ level. A possible reason could be that longitudinal variability combined with the rapid

Table 3. Observed energy fluxes

Exposures	Properties	Wavelength Å	Energy flux erg s ⁻¹ cm ⁻²	S/N	Spectral energy flux erg s ⁻¹ cm ⁻² Å ⁻¹
Exp 3	NUV: Mg II	2792.0 – 2807.0	$(9.3 \pm 0.57) \times 10^{-16}$	16.4	$(6.2 \pm 0.38) \times 10^{-17}$
Exp 4	NUV: Mg II	2792.0 – 2807.0	$(7.1 \pm 0.70) \times 10^{-16}$	10.1	$(4.7 \pm 0.47) \times 10^{-17}$
Exp 3+4	NUV: Mg II	2792.0 – 2807.0	$(8.2 \pm 0.46) \times 10^{-16}$	18.0	$(5.5 \pm 0.31) \times 10^{-17}$
Exp 3	NUV	2200.0 – 2700.0	$(1.7 \pm 0.35) \times 10^{-15}$	4.9	$(3.4 \pm 0.69) \times 10^{-18}$
Exp 4	NUV	2200.0 – 2700.0	$(1.2 \pm 0.35) \times 10^{-15}$	3.4	$(2.4 \pm 0.70) \times 10^{-18}$
Exp 3+4	NUV	2200.0 – 2700.0	$(1.4 \pm 0.24) \times 10^{-15}$	5.9	$(2.9 \pm 0.49) \times 10^{-18}$
Exp 3+4	NUV	2200.0 – 3150.0	$(3.9 \pm 0.58) \times 10^{-15}$	6.7	$(4.1 \pm 0.61) \times 10^{-18}$
Exp 1+2+6+7+8+9	Average FUV	1330.0 – 1710.0	$(1.9 \pm 1.3) \times 10^{-16}$	1.4	$(4.9 \pm 3.6) \times 10^{-19}$
Exp 5	Ly- α red wing	1215.85 – 1216.2	$(8.0 \pm 1.6) \times 10^{-16}$	4.9	$(2.3 \pm 0.47) \times 10^{-15}$

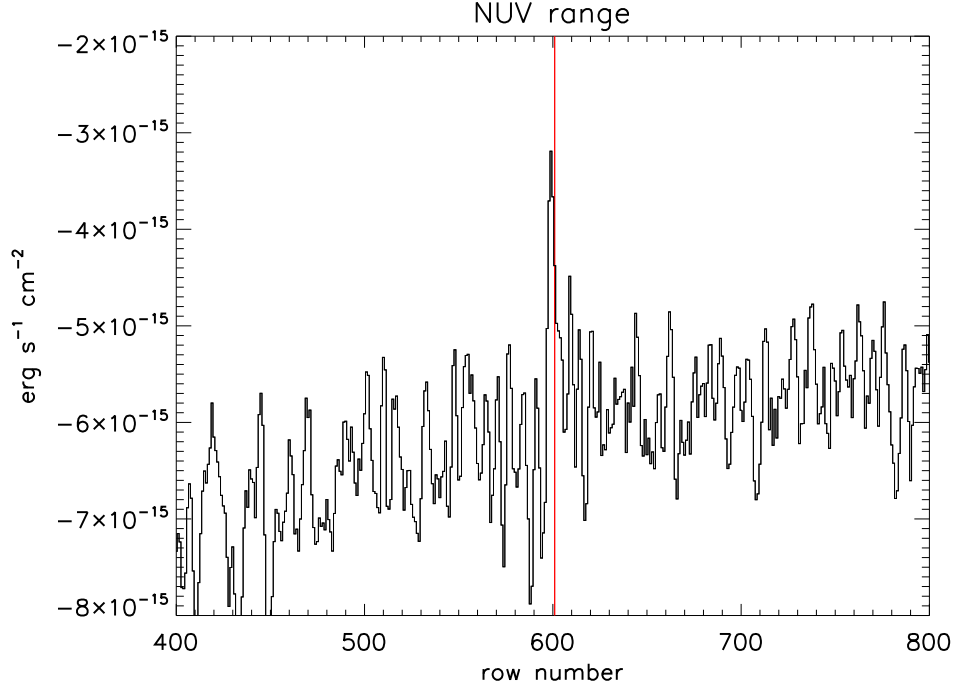


Figure 2. NUV flux integrated along the direction of dispersion as a function of the row number i_y to confirm location of target. The red vertical line shows the expected reference location of LSR J1835+3259. Note that the negative values of the background fluxes occurring in the x2d-files do not have physical meaning. They are due to the dark current correction within the STIS calibration pipeline of STScI generating the x2d-files. A detailed discussion of the dark current uncertainties in the NUV MAMA data can be found in section 4.1.3 of the STIS Data Handbook (Bostroem & Proffitt 2011). Only for the purpose of target confirmation within the background noise, we show here the original x2d data and do not remove these background fluxes in this figure.

rotation of the dwarf causes an apparent time-variability. Time-variability of emission at other wavelengths related to the dwarfs rotation have also been observed by Berger et al. (2008) and Hallinan et al. (2008, 2015). The spectrum contains significant flux between 2200 and 2700 Å with an averaged value of $(1.4 \pm 0.24) \times 10^{-15}$ erg s⁻¹ cm⁻² for both exposures combined with a S/N = 5.9 (see Table 3 and Figure 2). The flux within this wavelength range is by a factor of 1.4 ± 0.5 larger for exposure # 3 compared to exposure # 4. This ratio also points towards a time/longitudinal variability of the emission between both exposures. Due to the noisy data, it is however not possible to identify spectral features such as Fe II emission within this wavelength band.

In Figure 1, a spectral feature around 3065 Å is visible, which is marked with a red vertical line. The fluxes within the wavelength band 3060 – 3080 Å are significant with an S/N of approximately four. This feature around 3065 Å might be due TiO emission. According to Palmer & Hsu (1972), TiO possesses the most prominent features in the UV in a collection of bands within 2900-3260 Å. In laboratory experiments, Phatak & Palmer (1970) identify unclassified electronic transitions near 3062 Å and 2069 Å, which Palmer & Hsu (1972) measure at a slightly different wavelength of 3071 Å. TiO emission from LSR J1835+3259 would not be very surprising because TiO has been shown to be present on M-dwarfs (e.g., Bessell 1991; Johns-Krull & Valenti 1996), on brown dwarfs (e.g., Rebolo et al. 1996) and on hot Jupiters (e.g., Evans et al. 2016) through observations of absorption features.

3.2. Far-UV

Emission in the FUV is searched for with STIS grating G140L within the wavelength range 1150 Å to 1730 Å. Observations were taken during three visits with the original aim to resolve time-variability of the FUV emission (see Table 1). In Figure 4 we show the net fluxes as a function of wavelength for all six exposures and the average of all

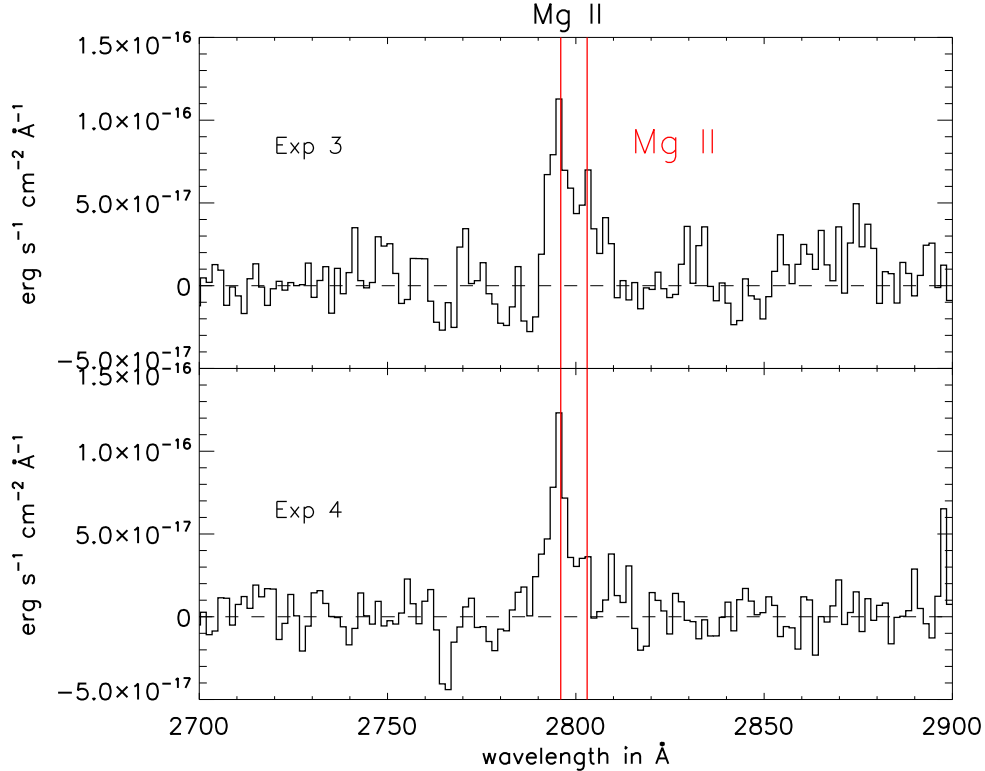


Figure 3. Mg II doublet for exposure # 3 and #4. The vertical red lines indicate the known position of the Mg II doublet at 2796 and 2803 Å (e.g., [Feldman et al. 1996](#); [France et al. 2013](#)).

exposures. The spectra are shifted vertically for readability, respectively. The fluxes contain spectral variability at longer wavelengths. This variability however appears to be mostly of statistical nature since the average spectrum is fairly flat. At 1304 Å and Ly- α wavelengths the spectrum is strongly contaminated by geocoronal emission.

Integrating the flux between 1330 Å and 1710 Å indicated by the green lines in Figure 4, we find a total flux of $(1.9 \pm 1.3) \times 10^{-16}$ erg s $^{-1}$ cm $^{-2}$. This flux cannot be considered significant because its uncertainty is similar to the flux. The uncertainty in the detection of a signal from LSR J1835+3259 is also evident in Figure 5. In this Figure we show the integrated flux between 1330 Å and 1710 Å as a function of row number where we added the flux of the neighboring row above and the one below, respectively, in order to reduce the scattering in the plot. The trace where LSR J1835+3259 is formally located is indicated with a red vertical line, which shows a very small local maximum. The existence of other larger maxima at neighboring rows however indicates that no FUV emission from LSR J1835+3259 can be identified with significance.

3.3. Lyman- α

During orbit 3, we searched for emission from the Ly- α wings of LSR J1835+3259 using the grating G140M and a very narrow slit of 0.05 arcsec. The resultant spectra are shown in Figure 6. In the top panel, we show in black the total spectrum along the trace, which includes rows with the target. Emission in the spectral vicinity of the Ly- α resonant emission line at 1215.67 Å is strongly altered by absorption in the interstellar medium and by geocoronal emission (e.g., [Linsky & Wood 1996, 2014](#); [Vidal-Madjar et al. 2003](#); [France et al. 2013](#)). The geocoronal Ly- α emission is displayed in Figure 6 as the green curve. It is calculated from rows not containing the target (see Table 2). The emission inside the wavelength range 1215.35 Å and 1215.85 Å, indicated as vertical dotted lines in Figure 6, is typically very significantly affected by absorption in the interstellar medium (e.g., [Linsky & Wood 2014](#)).

The net flux, i.e., the difference between the total flux and the geocoronal background is displayed in the lower panel of Figure 6 as red curve. In the red wing around 1216 Å a surplus is visible (both in the top and bottom panels). There is no significant net flux in the very noisy blue wing. The spectrum in the red wing yields values up $\sim 5 \times 10^{-15}$

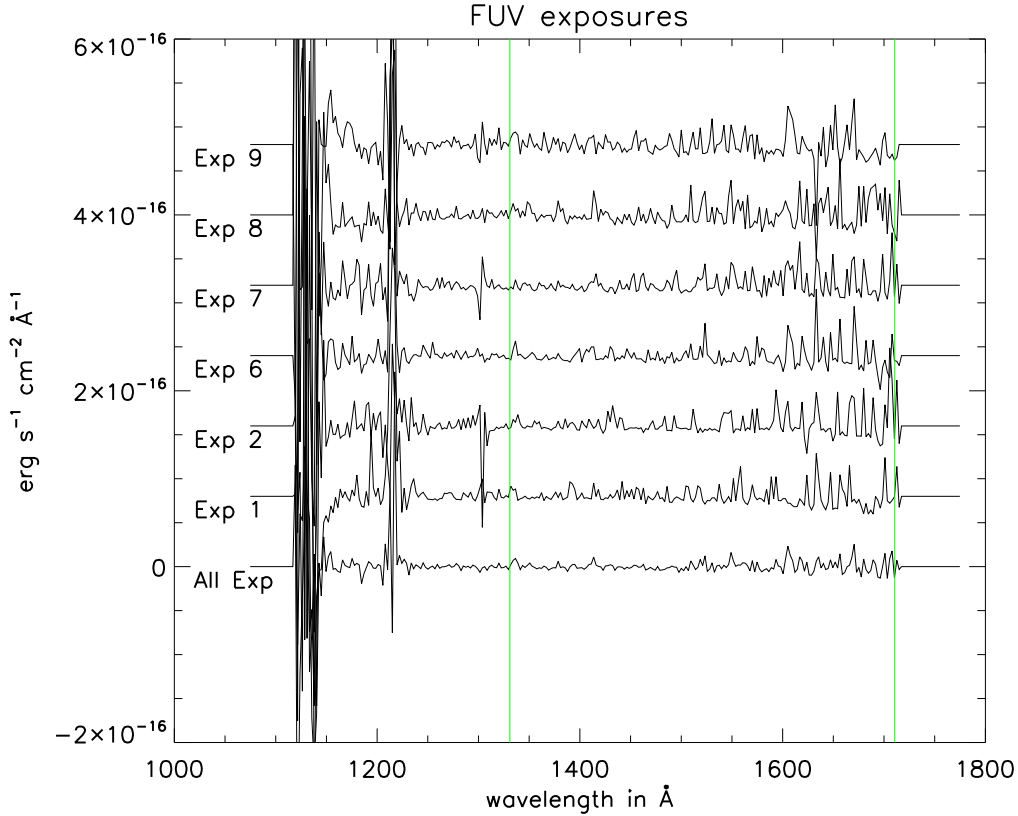


Figure 4. Net FUV flux along trace for all FUV exposures and average net flux from all FUV exposures. Fluxes for different exposures are shifted for visibility. The green vertical lines show the wavelength range over which total fluxes are calculated.

$\text{erg s}^{-1} \text{cm}^{-2} \text{\AA}^{-1}$ near 1215.9\AA . For the total integrated flux in the red wing between 1215.85\AA and 1216.2\AA we find $(8.0 \pm 1.6) \times 10^{-16} \text{erg s}^{-1} \text{cm}^{-2}$.

To independently test the significance of the surplus of emission in the Ly- α wings, we compute the total flux within the red wing between 1215.85\AA and 1216.2\AA in each row separately. The resultant integrated flux as a function of row number is shown in Figure 7. In the integration along a row we added the flux of the neighboring row above and the one below, respectively, in order to reduce the scattering in the plot. We see a local surplus of emission at the reference row indicated as red vertical line. The flux at the reference row is maximum even though smaller local maxima exist at other rows.

Based on the observations of the Ly- α fluxes in the red wing, we reconstruct the expected Ly- α source profile from LSR J1835+3259 similarly to previously applied approaches (e.g., Woods et al. 2005; France et al. 2013; Bourrier et al. 2015; Youngblood et al. 2016). We model the source profile with a Voigt profile with a Doppler width of 73 km s^{-1} and a damping parameter of 0.09 (similar to the values for the M3 star GJ 436 chosen by Bourrier et al. (2015)). Absorption in the interstellar medium by hydrogen H I and deuterium D I was calculated with a Lorentzian absorption profile with cross sections from, e.g., Morton (2003) and Wiese & Fuhr (2009), and a Maxwell-Boltzmann velocity distribution of the interstellar gas with an adjusted Gaussian standard deviation of $\sigma_H = 12 \text{ km s}^{-1}$. The ratio of D I to H I was assumed to be 1.5×10^{-5} and standard deviation of deuterium σ_D to be a factor of $\sqrt{2}$ smaller compared to σ_H (Woods et al. 2005). The convolution of both the Lorentzian and Gaussian profiles leads to a Voigt profile. The relative radial velocity between the interstellar medium and LSR J1835+3259 is 22.9 km s^{-1} based on heliospheric velocities of the dwarf of 8.4 km s^{-1} (Deshpande et al. 2012) and velocities of -14.4 km s^{-1} of the interstellar medium using the LISM kinetic calculator¹ (Redfield & Linsky 2008). The resultant Ly- α profile was convolved with the line spread function described in the STIS Instrument Handbook (Riley et al. 2017). We find a good fit to the observations

¹ <http://sredfield.web.wesleyan.edu/>

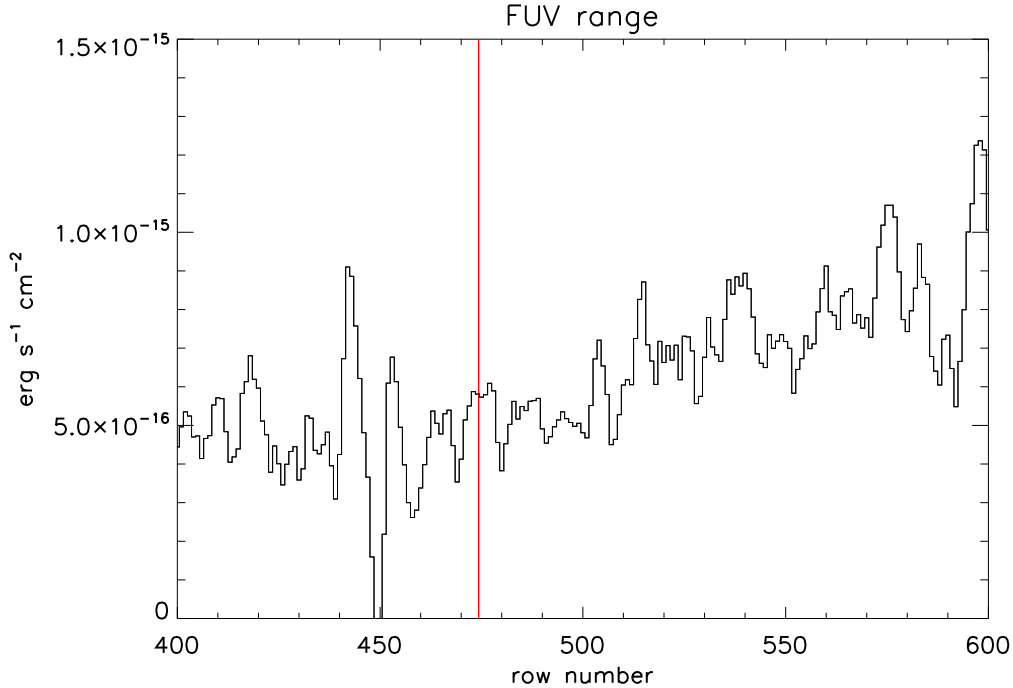


Figure 5. FUV flux integrated along direction of dispersion as a function of the row number. The red vertical line shows the expected reference location of LSR J1835+3259.

shown as black line in Figure 7 with a source Voigt profile with amplitude $1.2 \times 10^{-14} \text{ erg s}^{-1} \text{ cm}^{-2} \text{ \AA}^{-1}$ and an H I column density of $1 \times 10^{18} \text{ cm}^{-2}$. We see that the red wing of the observations is well reproduced by the fit. The total reconstructed Ly- α profile is shown as the blue dotted lines in Figure 7. The total integrated Ly- α source flux is $7.0 \times 10^{-15} \text{ erg s}^{-1} \text{ cm}^{-2}$. We note that there is a partial degeneracy in the reconstruction of the source profile because different combinations of the main free parameters, i.e., interstellar column densities, temperatures and source profile shapes, can lead to similar transmission profiles agreeing with the noisy observations. Exploring this parameter space we find that an uncertainty on the order of a factor of two to three remains in constraining the integrated Ly- α source flux.

As a simple independent check of our reconstructed total Ly- α flux source flux, we alternatively use the observed and reconstructed Ly- α profiles of three M2 and later dwarfs studied by France et al. (2013). The Ly- α spectra of these three dwarfs are red wing dominated similar to the spectrum of LSR J1835+3259. The dwarfs GJ 581 (M2.5), GJ 876 (M4), and GJ 436 (M3) have fluxes at 1216.0 \AA of ~ 8 , ~ 9 and $\sim 9 \times 10^{-14} \text{ erg s}^{-1} \text{ cm}^{-2} \text{ \AA}^{-1}$, respectively. The total reconstructed Ly- α emission from these stars by France et al. (2013) is 3.0 , 4.4 and $3.5 \times 10^{-13} \text{ erg s}^{-1} \text{ cm}^{-2}$, respectively. This results in a ratio of ~ 4 between the total Ly- α flux and the flux per \AA at 1216 \AA . At LSR J1835+3259 we measure a spectral flux of approximately $3 \times 10^{-15} \text{ erg s}^{-1} \text{ cm}^{-2}$ at 1216.0 \AA . Extending the scaling from the three M-dwarfs to LSR J1835+3259, we expect a total Ly- α flux of $1.2 \times 10^{-14} \text{ erg s}^{-1} \text{ cm}^{-2}$, which is within 40% of the modeled value of the previous paragraph. The signal to noise of our observed red wing flux is five. But due to the partial degeneracy in the reconstruction processes of the the total source flux, the total Ly- α flux should be considered reasonable within a factor of two or three.

4. IMPLICATIONS

In this section we compare the observed UV spectrum of LSR J1835+3259 with the spectrum of Jupiter’s auroral emission and the UV spectra of three low mass stars of spectral type M4.5 and later.

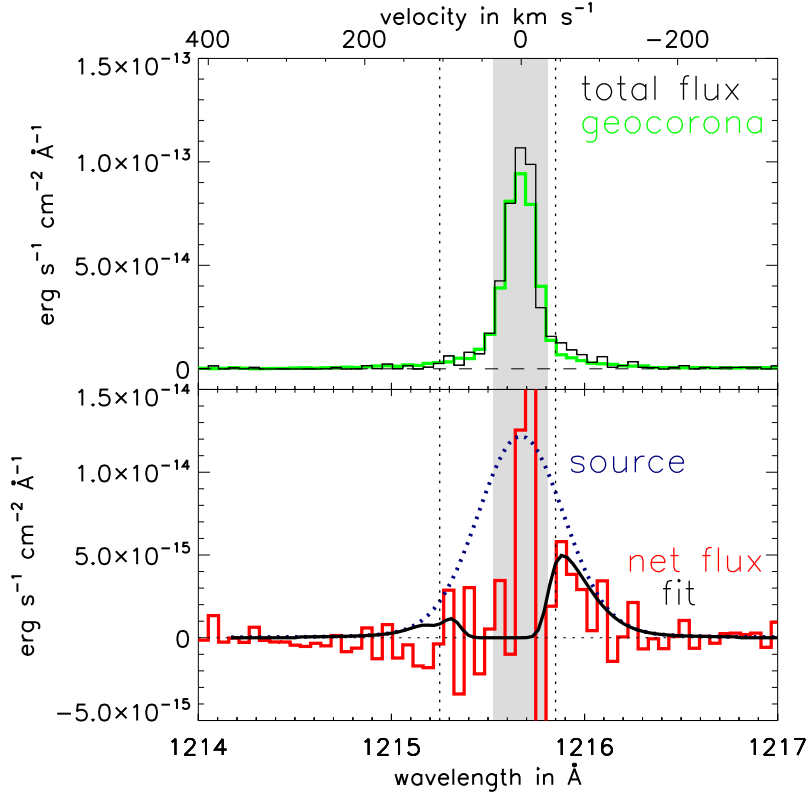


Figure 6. Ly- α fluxes. Top panel shows total Ly- α flux in black and geocoronal emission as green line. Bottom panel shows net Ly- α flux in red. Wavelengths between the dotted vertical lines indicate where the target emission experiences very significant absorption in the interstellar medium. The blue dotted curve is the reconstructed source Ly- α profile. The black solid lines is a fit to the data calculated by considering absorption of H I and D I in the interstellar medium. The grey shaded area shows the wavelength range heavily contaminated by geocoronal emission.

4.1. Comparison with Jupiter's auroral emission

The Balmer H- α emission and emission at radio wavelengths from LSR J1835+3259 have been interpreted by Hallinan et al. (2015) as auroral emission caused by electron beams originating within the magnetosphere of LSR J1835+3259. The emission of the dwarf could therefore be an upscaled version of the auroral emission of Jupiter. To test this hypothesis we compare luminosities at optical and UV wavelengths of LSR J1835+3259 with those of Jupiter

Table 4. Luminosities in erg s^{-1} for different wavelength ranges: LSR J1835+3259, Jupiter and mid/late-type M-dwarf stars compared. (1): Hallinan et al. (2015), (2): Bhardwaj & Gladstone (2000), (3): Pryor et al. (1998), (4): Broadfoot et al. (1981); Gladstone et al. (2002), (5): Based on the uncertainty to reconstruct the Ly- α source flux (see Section 3.3), (6): France et al. (2016). Value ranges for Jupiter represent observed time-variability.

	Type	H- α	NUV without Mg II	Mg II	FUV without Ly- α	Ly- α
LSR J1835+3259	M8.5	2.5×10^{24} (1)	$(1.2 \pm 0.2) \times 10^{25}$	$(3.2 \pm 0.2) \times 10^{24}$	$\leq 7.3 \times 10^{23}$	$(2.7^{+5.4}_{-1.8}) \times 10^{25}$ (5)
Jupiter	–	$1 - 10 \times 10^{17}$ (2)	$1 - 10 \times 10^{18}$ (3)	–	$1 - 5 \times 10^{19}$ (4)	$1 - 5 \times 10^{19}$ (2)
GJ 581 (6)	M5	–	2.8×10^{27}	8.9×10^{25}	8.1×10^{25}	5.5×10^{26}
GJ 876 (6)	M5	–	2.2×10^{27}	8.3×10^{25}	4.2×10^{26}	1.0×10^{27}
GJ 1214 (6)	M4.5V	–	8.5×10^{26}	4.2×10^{25}	7.5×10^{25}	4.3×10^{26}

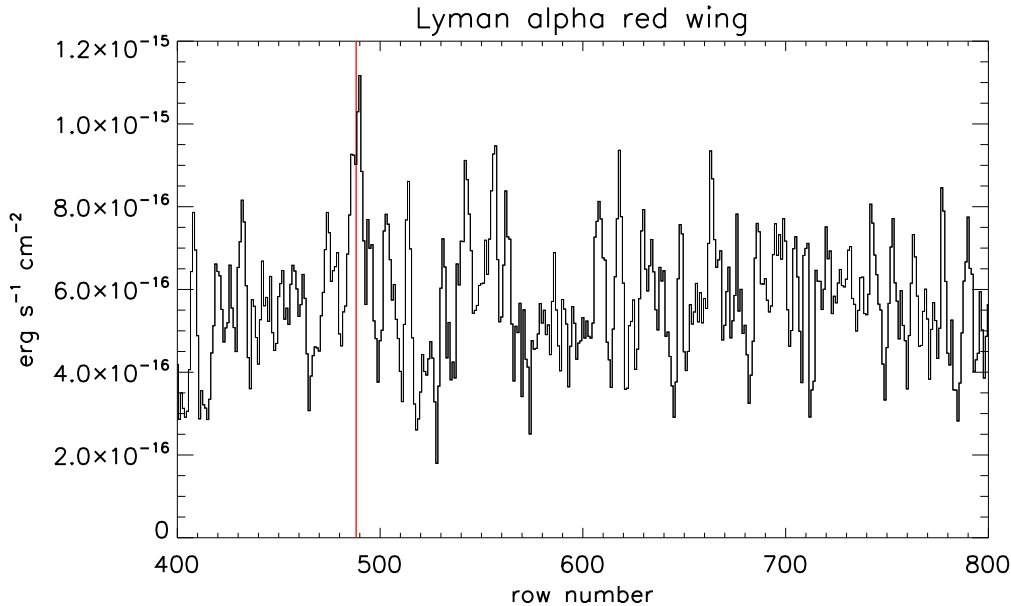


Figure 7. Integrated flux within Ly- α wing within 1215.85 and 1216.2 Å as a function of row number. The red vertical line shows the expected reference location of LSR J1835+3259.

in Figure 8(a) and in Table 4. The black diamonds display the measured luminosities of Jupiter’s aurora at H- α , the NUV, FUV, and Ly- α . In our comparison, we show the luminosities of Mg II and Ly- α , separately, and therefore exclude their emission in the displayed NUV and FUV bands, respectively. We multiplied the Jovian luminosities by a factor of $\sim 10^7$ for a better comparison with those of LSR J1835+3259. In that way luminosities at the H- α wavelength are comparable for Jupiter and LSR J1835+3259 in Figure 8(a). The observed variability of Jupiter’s emission at the various wavelength ranges listed in Table 4 is indicated as error bars in Figure 8(a). The uncertainties of the luminosities of LSR J1835+3259 derived in the previous section are included as well.

The Jovian luminosities increase roughly by a factor of 10 from H- α to the NUV with most of the emission in the NUV stemming from hydrogen. The auroral luminosity increases again roughly by a factor of 10 to the FUV, where the power is split almost evenly between the Ly- α emission and other wavelengths in the FUV. The luminosity of LSR increases by a factor of five from the H- α emission to the NUV. Roughly 1/4 of the NUV stems from the Mg II emission, the other emission is uncertain. It could be partially due to TiO, but could contain contributions, e.g., from Fe II lines as seen in M-dwarfs (e.g., France et al. 2013) or from hydrogen. In the FUV between 1330 and 1710 Å we find values of $7.3 \pm 5.2 \times 10^{23}$ erg s $^{-1}$. The flux is very weak and at the detection threshold. The derived FUV luminosities therefore should be considered upper limits. Based on the assumption that LSR J1835+3259 scales similarly to Jupiter throughout the optical and UV, the dwarf, however, fails by a factor of approximately 1000 to reproduce Jupiter in the FUV wavelength range without Ly- α . At Ly- α wavelength, LSR J1835+3259 scales about a factor of 10 weaker compared to Jupiter.

Jupiter’s UV spectrum contains the Mg II doublet at 2800 Å, but it originates from reflectance of the solar Mg II emission. To the authors’ knowledge, Mg II in emission from Jupiter was only seen in connection with the collision of comet Shoemaker-Levy 9. After the collision of the comet’s G fragment, emission from Jupiter’s stratosphere was reported by Noll et al. (1995) and an outburst of Mg II was observed before collision when the comet was inside Jupiter’s magnetosphere (Feldman et al. 1996). Due to absence of observed Mg II emission intrinsic to Jupiter we do not include Mg II in the comparison in Figure 8(a).

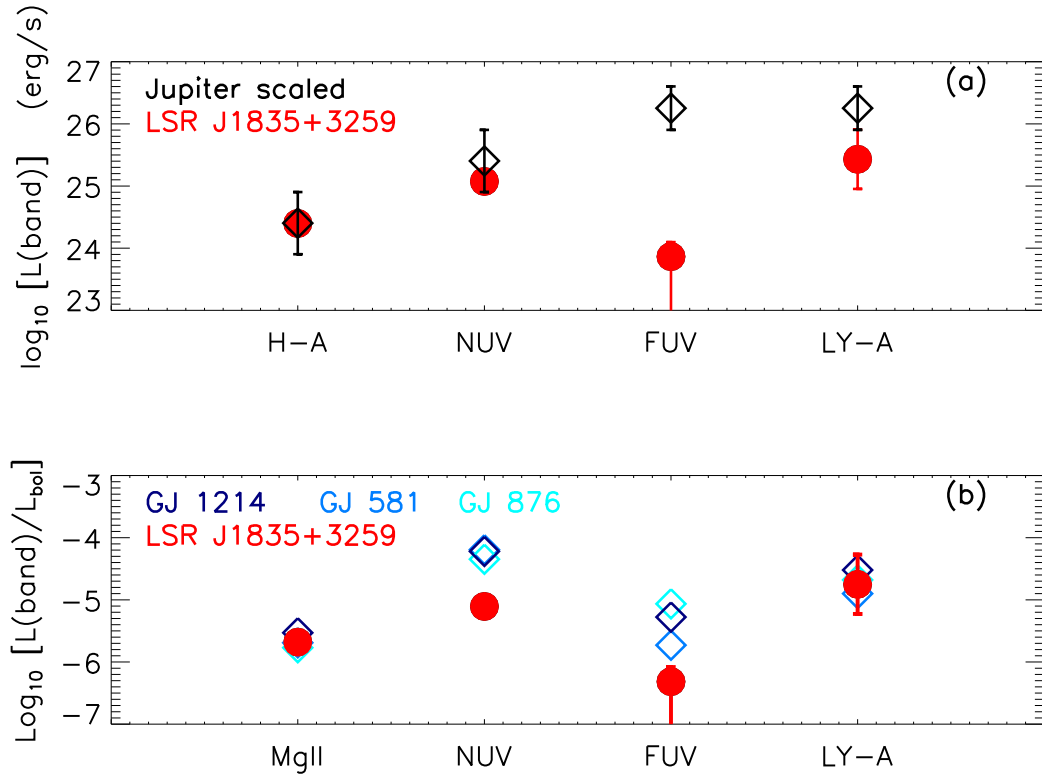


Figure 8. Luminosities of LSR J1835+3259 for selected wavelength ranges in comparison with Jupiter in panel (a) and with three late M-dwarf stars in panel (b). Mg II is excluded from the NUV band and Ly- α is excluded from the FUV band in both panels. Panel (a): Jupiter is scaled to LSR J1835+3259 at H- α wavelength. Bottom Panel (b): LSR J1835+3259 compared with GJ 581, GJ 876, and GJ 1214 but scaled to their respective bolometric luminosities (see also Table 4). Error bars on the luminosities of LSR J1835+3259 include statistical errors and the uncertainty from reconstructing the Ly- α source flux. When error bars are not visible, they are smaller than the used symbols (for exact values see Table 4). Error bars on the values for Jupiter do not represent measurement errors, but observed temporal-variability (see text and table 4). Measurement errors for the M-dwarfs are not explicitly provided in table 3 of France et al. (2016), but should be 30% or smaller based on France et al. (2013).

4.2. Comparison with M-dwarfs

In Figure 8 (b), we compare the luminosity of LSR J1835+3259 with those of the three dwarf stars GJ 876, GJ 581 and GJ 1214, which are of spectral type M4.5 and later. For these stars UV spectra have been previously obtained with HST (France et al. 2013, 2016; Youngblood et al. 2016, 2017; Loyd et al. 2016). We compare the targets normalized to their bolometric luminosities, respectively (see France et al. (2016)). Due to the absence of H- α in emission from these dwarfs, we do not include H- α in panel (b) of Figure 8. Because we display the luminosities of Mg II and Ly- α , separately, we exclude the luminosities of these two wavelengths in the NUV and FUV bands, respectively.

From the absolute values of the luminosities listed in Table 4, we find that LSR J1835+3259 is about a factor of 200 less luminous in the NUV range and about a factor of 30 less luminous at Ly- α and Mg II wavelengths compared to the M5 dwarfs GJ 581 and GJ 876. However, taking the luminosity of LSR J1835+3259 and the three M-dwarfs with respect to their individual bolometric luminosities, we find that the line luminosities of Mg II and Ly- α scale very similarly for all four objects. The Ly- α to Mg II luminosity ratio for LSR J1835+3259 is 10 with a statistical uncertainty of ± 2 (plus the additional systematic uncertainty from the reconstruction of the Ly- α source profile discussed in Section 3.3). France et al. (2013) derive a similar ratio of 10 ± 3 between the Ly- α luminosity and the luminosity of the Mg II doublet for M-dwarfs (including the three M-dwarfs considered here). Comparable ratios also follow from the scaling laws derived by Shkolnik et al. (2014).

For LSR J1835+3259, the Ly- α luminosity comprises about 70%, i.e., a large fraction, of its total UV luminosity. This ratio is within the range of 37% to 75% for M-dwarfs derived by [France et al. \(2013\)](#). The relative NUV luminosities of the three M-dwarfs (excluding Mg II) are slightly less than a factor of 10 smaller compared to LSR J1835+3259. The relative FUV luminosity (without Ly- α) of LSR J1835+3259 are a factor of 7 to 50 smaller compared to those of the M-dwarfs.

In addition to the mid-M-dwarfs of the previous section, it is also interesting to compare the late-type M8 dwarf-star Trappist-1 with the M8.5 dwarf LSR J1835+3259, which are both of very similar spectral type. The Ly- α luminosity of Trappist-1 is 1.4×10^{26} erg s $^{-1}$ as recently determined by [Bourrier et al. \(2017a\)](#). Trappist-1 is therefore approximately a factor of three brighter at Ly- α wavelength compared to LSR J1835+3259. Trappist-1 thus lies in its absolute Ly- α luminosity in-between LSR J1835+3259 and the discussed mid-dwarfs, which are a factor of 30 brighter. These observations thus confirm the trend of decreasing Ly- α luminosity with increasing spectral type.

Summarizing the main findings of this subsection we see that LSR J1835+3259 is very similar to mid-M-dwarfs in their Mg II and Ly- α luminosities when normalized to their respective bolometric luminosity. We also find that the Ly- α luminosity dominates the total FUV luminosity, both, in case of LSR J1835+3259 and in case of the three M-dwarfs.

5. CONCLUSIONS AND DISCUSSION

In the previous section we compared the UV spectrum of LSR J1835+3259 with the auroral UV spectrum of Jupiter and the spectra of mid/late M-dwarf stars. We find that the observed luminosities of LSR J1835+3259 in the UV are not consistent with an auroral spectrum expected from Jupiter due to the factor of 1000 discrepancy at FUV wavelengths (without Ly- α). In addition, the emission at Ly- α is lower by approximately a factor of 10 compared to the averaged relative Ly- α luminosity of Jupiter. The error bars at Ly- α wavelength however marginally overlap, where in the case of Jupiter the error bars do not represent measurement uncertainties but observed time-variability.

The emission of LSR J1835+3259 resembles those of late-type M-stars very well when considering the Mg II to Ly- α ratio. We also see that the FUV luminosities (without Ly- α) is smaller than the Ly- α luminosity for LSR J1835+3259 as well as for the three \sim M5 dwarfs, where UV spectra are available ([France et al. 2013, 2016](#); [Youngblood et al. 2016](#); [Loyd et al. 2016](#)). This is not the case for Jupiter, where there is an approximate equipartition in Ly- α and the FUV band (without Ly- α) ([Bhardwaj & Gladstone 2000](#)).

The luminosity in the NUV and FUV bands of LSR J1835+3259 (without Mg II and Ly- α , respectively) is, however, about an order of magnitude smaller compared to the three mid-type M-dwarfs considered here. In case of these M-dwarf stars emission from C II, Si IV, C IV, and C I is detected in their FUV spectra and Fe II lines in their NUV spectra ([France et al. 2013](#)). These lines could not be identified in the spectrum of LSR J1835+3259 even though they might contribute to the observed fluxes in these wavelength ranges. The reason for the weakness of these lines in LSR J1835+3259 is unclear. It could be a property of the later spectral type and its resultant chromospheric structure, i.e. M8.5, of LSR J1835+3259 compared to the M4.5 and M5 dwarfs. It might be alternatively caused by different chromospheric flare activity levels. For LSR J1835+3259 flare activity is observed at H- α , while the three M-dwarf stars display weak chromospheric activity and H- α is in absorption ([Gizis et al. 2002](#); [Berger et al. 2008](#); [Hallinan et al. 2015](#); [France et al. 2013, 2016](#); [Reiners et al. 2018](#)).

Based on this comparison the overall impression is that the dwarf LSR J1835+3259 exhibits radiative properties which are generally more similar to those of low mass stars than that of massive planets with externally driven auroral emission. A significant part of the emission from LSR J1835+3259 might therefore be generated by internal processes. Such processes could be chromospheric and coronal heating driven by intrinsic magnetic activity, which results in reconnection or wave heating (e.g., [Kuzmychov et al. 2017](#); [Berdyugina et al. 2017](#)).

It is worthwhile to point out that the heating and emission from quiescent chromospheres is in general not a well understood process. In particular the ratio of the two primarily discussed processes, i.e., mini-flares or wave-particle interaction due to turbulent plasma waves, is being debated in the literature (e.g., [Güdel 1997](#); [Güdel et al. 2003](#); [Airapetian & Holman 1998](#)). But even observational evidence for electron beam generated emission from ultracool dwarfs might not uniquely demonstrate the existence of auroral processes caused by external power generators as in case of the planets in the solar system. For example, observed emissions of the transition region and chromosphere of the sun provide evidence of heating by electron beams generated by nano-flare events (e.g., [Testa et al. 2014](#); [Reep et al. 2015](#); [Dudík et al. 2017](#)).

Even though our observations of LSR J1835+3259 are not consistent with auroral activity similar to those on Jupiter, we cannot entirely rule out that the emission of this dwarf contains auroral emission, i.e., emission driven by electron or ion beams generated within the magnetosphere of the dwarf. The space and plasma environment around ultracool dwarfs is not sufficiently well understood. Therefore possible electron energization mechanisms, resulting electron energy distributions, locations of electron energy deposition within the chromosphere and the resultant expected emission spectra throughout the electromagnetic wavelengths range are not well constrained. The nature and occurrence of UV emission and aurora from ultracool dwarfs is thus a complex topic because the emission is controlled by various physical parameters. The emission depends on intrinsic parameters such as their magnetic fields and atmospheres, but it might also depend on unknown external generators, which could power aurora.

This work is based on observations with the NASA/ESA Hubble Space Telescope obtained at the Space Telescope Science Institute, which is operated by the Association of Universities for Research in Astronomy (AURA), Inc., under NASA contract NAS 5-26555. We thank J. Debes for helpful comments on the scheduling and data processing of the observations. CF and JS acknowledge funding by Verbundforschung für Astronomie und Astrophysik through grant number 50 OR 170. The work at Johns Hopkins University was supported by NASA through grant HST-GO-14617.002-A from the Space Telescope Science Institute.

REFERENCES

- Airapetian, V. S., & Holman, G. D. 1998, *Astrophys. J.*, 501, 805
- Basri, G. 2000, *ARA&A*, 38, 485
- Basri, G. 2014, in *Astrophysics and Space Science Library*, Vol. 401, 50 Years of Brown Dwarfs, ed. V. Joergens, 51
- Berdugina, S. V., Harrington, D. M., Kuzmychov, O., et al. 2017, *Astrophys. J.*, 847, 61
- Berger, E., Basri, G., Gizis, J. E., et al. 2008, *Astrophys. J.*, 676, 1307
- Bessell, M. S. 1991, *Astron. J.*, 101, 662
- Bhardwaj, A., & Gladstone, G. R. 2000, *Rev. Geophys.*, 38, 295
- Bonfond, B., Grodent, D., Badman, S. V., et al. 2017, *Icarus*, 292, 208
- Bostroem, K., & Proffitt, C. 2011, *STIS Data Handbook*, Baltimore: STScI
- Bourrier, V., Ehrenreich, D., & Lecavelier des Etangs, A. 2015, *A&A*, 582, A65
- Bourrier, V., Ehrenreich, D., Wheatley, P. J., et al. 2017a, *A&A*, 599, L3
- Bourrier, V., de Wit, J., Bolmont, E., et al. 2017b, *AJ*, 154, 121
- Broadfoot, A. L., et al. 1981, *J. Geophys. Res.*, 86, 8259
- Clarke, J. T., Trauger, J., & Waite, J. H. 1989, *Geophys. Res. Lett.*, 16, 587
- Clarke, J. T., Ben Jaffel, L., Vidal-Madjar, A., et al. 1994, *ApJL*, 430, L73
- Clarke, J. T., Ajello, J., Ballester, G. E., et al. 2002, *Nature*, 415, 997
- Cohen, O., Drake, J. J., Kashyap, V. L., et al. 2009, *ApJL*, 704, L85
- Connerney, J. E. P., Baron, R., Satoh, T., & Owen, T. 1993, *Science*, 262, 1035
- Crossfield, I. J. M., Biller, B., Schlieder, J. E., et al. 2014, *Nature*, 505, 654
- Cuntz, M., Saar, S. H., & Musielak, Z. E. 2000, *ApJL*, 533, L151
- Deshpande, R., Martín, E. L., Montgomery, M. M., et al. 2012, *AJ*, 144, 99
- Dudík, J., Džifčáková, E., Meyer-Vernet, N., et al. 2017, *SoPh*, 292, 100
- Ebert, R. W., Allegrini, F., Bagenal, F., et al. 2017, *Geophys. Res. Lett.*, 44, 9199
- Evans, T. M., Sing, D. K., Wakeford, H. R., et al. 2016, *Astrophys. J. Lett.*, 822, L4
- Feldman, P. D., Weaver, H. A., Boice, D. C., & Stern, S. A. 1996, *Icarus*, 121, 442
- France, K., Linsky, J. L., Tian, F., Froning, C. S., & Roberge, A. 2012, *Astrophys. J. Lett.*, 750, L32
- France, K., Froning, C. S., Linsky, J. L., et al. 2013, *Astrophys. J.*, 763, 149
- France, K., Loyd, R. O. P., Youngblood, A., et al. 2016, *Astrophys. J.*, 820, 89
- Gillon, M., Jehin, E., Lederer, S. M., et al. 2016, *Nature*, 533, 221
- Gizis, J. E., Reid, I. N., & Hawley, S. L. 2002, *Astron. J.*, 123, 3356
- Gladstone, G. R., Waite, J. H., Grodent, D., et al. 2002, *Nature*, 415, 1000
- Güdel, M. 1997, *ApJL*, 480, L121
- Güdel, M., Audard, M., Kashyap, V. L., Drake, J. J., & Guinan, E. F. 2003, *Astrophys. J.*, 582, 423

- Hallinan, G., Antonova, A., Doyle, J. G., et al. 2008, *ApJ*, 684, 644
- Hallinan, G., Littlefair, S. P., Cotter, G., et al. 2015, *Nature*, 523, 568
- Hawley, S. L., & Johns-Krull, C. M. 2003, *Astrophys. J. Lett.*, 588, L109
- Helling, C., & Casewell, S. 2014, *Astron. Astrophys. Rev.*, 22, 80
- Hill, T. W. 2001, *J. Geophys. Res.*, 106, 8101
- Ip, W.-H., Kopp, A., & Hu, J. 2004, *Astrophys. J.*, 602, L53
- Johns-Krull, C. M., & Valenti, J. A. 1996, *Astrophys. J. Lett.*, 459, L95
- Kuzmychov, O., Berdyugina, S. V., & Harrington, D. M. 2017, *Astrophys. J.*, 847, 60
- Lanza, A. F. 2009, *A&A*, 505, 339
- Lépine, S., Rich, R. M., & Shara, M. M. 2003, *AJ*, 125, 1598
- Linsky, J. L., & Wood, B. E. 1996, *ApJ*, 463, 254
- . 2014, *ASTRA Proceedings*, 1, 43
- Loyd, R. O. P., France, K., Youngblood, A., et al. 2016, *Astrophys. J.*, 824, 102
- Mauk, B. H., & Bagenal, F. 2012, in *Geophysical Monograph Series 197 (American Geophysical Union)*, 3
- Mauk, B. H., Haggerty, D. K., Paranicas, C., et al. 2017, *Geophys. Res. Lett.*, 44, 4410
- Morton, D. C. 2003, *ApJS*, 149, 205
- Nichols, J. D., Burleigh, M. R., Casewell, S. L., et al. 2012, *ApJ*, 760, 59
- Noll, K. S., McGrath, M. A., Trafton, L. M., et al. 1995, *Science*, 267, 1307
- Palmer, H. B., & Hsu, C. J. 1972, *J. Molecular Spectroscopy*, 43, 320
- Phatak, C. M., & Palmer, H. B. 1970, *J. Molecular Spectroscopy*, 33, 137
- Pineda, J. S., Hallinan, G., & Kao, M. M. 2017, *Astrophys. J.*, 846, 75
- Poppenhaeger, K., & Schmitt, J. H. M. M. 2011, *ApJ*, 735, 59
- Prangé, R., Rego, D., Pallier, L., et al. 1997, *ApJL*, 484, L169
- Preusse, S., Kopp, A., Büchner, J., & Motschmann, U. 2005, *Astron. Astrophys.*, 434, 1191
- Pryor, W. R., Ajello, J. M., Tobiska, W. K., et al. 1998, *J. Geophys. Res.*, 103, 20149
- Rebolo, R., Martin, E. L., Basri, G., Marcy, G. W., & Zapatero-Osorio, M. R. 1996, *Astrophys. J. Lett.*, 469, L53
- Redfield, S., & Linsky, J. L. 2008, *ApJ*, 673, 283
- Reep, J. W., Bradshaw, S. J., & Alexander, D. 2015, *Astrophys. J.*, 808, 177
- Reid, I. N., Cruz, K. L., Laurie, S. P., et al. 2003, *AJ*, 125, 354
- Reiners, A., & Basri, G. 2008, *ApJ*, 684, 1390
- . 2009, *ApJ*, 705, 1416
- . 2010, *ApJ*, 710, 924
- Reiners, A., Zechmeister, M., Caballero, J. A., et al. 2018, *ArXiv e-prints*, arXiv:1711.06576
- Riley, A., et al. 2017, *STIS Instrument Handbook*, Baltimore: STScI
- Saur, J. 2017, in *Handbook of Exoplanets*, ed. H. J. Deeg & J. A. Belmonte (Springer), 1–17
- Saur, J., Grambusch, T., Duling, S., Neubauer, F. M., & Simon, S. 2013, *Astron. Astrophys.*, 552, A119
- Saur, J., Pouquet, A., & Matthaeus, W. 2003, *Geophys. Res. Lett.*, 30(5), 1260, doi:10.1029/2002GL015761
- Schrijver, C. J. 2009, *Astrophys. J. Lett.*, 699, L148
- Shkolnik, E., Bohlender, D. A., Walker, G. A. H., & Collier Cameron, A. 2008, *ApJ*, 676, 628
- Shkolnik, E., Walker, G. A. H., & Bohlender, D. A. 2003, *ApJ*, 597, 1092
- Shkolnik, E. L., Rolph, K. A., Peacock, S., & Barman, T. S. 2014, *ApJL*, 796, L20
- Strugarek, A., Brun, A. S., Matt, S. P., & Réville, V. 2015, *ApJ*, 815, 111
- Testa, P., De Pontieu, B., Allred, J., et al. 2014, *Science*, 346, 1255724
- Turnpenney, S., Nichols, J. D., Wynn, G. A., & Casewell, S. L. 2017, *MNRAS*, 470, 4274
- Vidal-Madjar, A., Lecavelier des Etangs, A., Désert, J.-M., et al. 2003, *Nature*, 422, 143
- Walkowicz, L. M., & Hawley, S. L. 2009, *Astron. J.*, 137, 3297
- Walkowicz, L. M., Johns-Krull, C. M., & Hawley, S. L. 2008, *Astrophys. J.*, 677, 593
- Wannawichian, S., Clarke, J. T., & Nichols, J. D. 2010, *Journal of Geophysical Research (Space Physics)*, 115, A02206
- Wiese, W., & Fuhr, J. 2009, *J. Phys. Chem. Ref. Data*, 38, 565
- Woods, T. N., Eparvier, F. G., Bailey, S. M., et al. 2005, *Journal of Geophysical Research (Space Physics)*, 110, 1312
- Youngblood, A., France, K., Loyd, R. O. P., et al. 2016, *Astrophys. J.*, 824, 101
- . 2017, *Astrophys. J.*, 843, 31
- Zarka, P. 1998, *J. Geophys. Res.*, 103, 20159